







## PAPER

[View Article Online](#)  
[View Journal](#) | [View Issue](#)Cite this: *Catal. Sci. Technol.*, 2022,  
12, 5657Understanding catalyst deactivation during the  
direct cracking of crude oil†Mohammed A. Alabdullah,<sup>a</sup> Tuiana Shoinkhorova,<sup>a</sup> Alla Dikhtiarenko,<sup>a</sup>  
Samy Ould-Chikh, <sup>a</sup> Alberto Rodriguez-Gomez,<sup>a</sup> Sang-ho Chung,<sup>a</sup>  
Arwa O. Alahmadi,<sup>a</sup> Idoia Hita, <sup>a</sup> Sébastien Pairis,<sup>b</sup> Jean-louis Hazemann, <sup>b</sup>  
Pedro Castaño, <sup>a</sup> Javier Ruiz-Martinez, <sup>a</sup> Isidoro Morales Osorio,<sup>c</sup>  
Khalid Almajnoui,<sup>c</sup> Wei Xu<sup>c</sup> and Jorge Gascon <sup>\*a</sup>

The increasing demand for base chemicals *i.e.*, ethylene and propylene, along with the expected peak in gasoline and fuels demand, are stirring intense research into refineries to be built around processes that maximize the production of chemicals (oil to chemicals, OTC, processes). One of the main challenges at hand for OTC technologies is the formulation of appropriate catalysts able to handle the wide boiling point of the feed and to withstand continuous operation at industrial scale. Hydrothermal degradation, coke deposition and the presence of impurities, such as metals, sulfur and nitrogen containing species, in the feedstock affect catalyst lifetime, activity and selectivity. In this work, we evaluate long term catalyst stability along with the main causes of reversible and irreversible catalyst deactivation. Our results demonstrate that formulation prevents, to a large extent, the degradation of the zeolitic components of the catalyst. Metal deposition, on the other hand, results in a slight decrease in activity along with partial changes in selectivity patterns. The main reasons behind these changes are discussed in detail with the help of extensive characterization.

Received 24th June 2022,  
Accepted 2nd August 2022

DOI: 10.1039/d2cy01125e

[rsc.li/catalysis](https://rsc.li/catalysis)

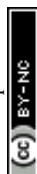
## Introduction

For more than one century, crude oil has been used as feedstock to produce fuels.<sup>1</sup> However, with the growth in environmental concerns, the development of more efficient combustion engines, and the growing markets of alternative engines (fully electric, hybrid, or H<sub>2</sub> powered), there is a common agreement that the fuel market is, in the long run, going to decrease in size. In contrast, the chemicals market still has room to grow. According to BP's 2022 Energy Outlook, oil demand will peak in 2025.<sup>2</sup> Oil consumed by industry, buildings, and power will also slump. However, the consumption of chemicals is expected to grow, from 16% of oil demand in 2020 to 34% by 2040.<sup>3</sup>

Refineries will be then built around processes that maximize the production of chemicals and minimize energy consumption (oil to chemicals, OTC, processes), in contrast

to the current state of the art where oil is first fractionated, and resulting streams are treated separately to manufacture an extensive portfolio of products. Several OTC processes have been reported in the literature, mainly based on modern steam crackers, fluidized catalytic crackers (FCC), and hydroprocessing technologies, as recently reviewed by Gascon *et al.*,<sup>3</sup> Bogle,<sup>4</sup> and Corma *et al.*<sup>5</sup> Commercial units have been recently commissioned or are under construction in China and the Middle East.<sup>6</sup> Since 2014, ExxonMobil is operating a pretreated light crude oil steam cracker in Singapore.<sup>7</sup> Saudi Arabia is also developing its own OTC portfolio.<sup>8,9</sup> For instance, Saudi Aramco is involved in several joint development processes with Axens, TechnipFMC, McDermott, and Chevron Lummus Global to commercialize its Thermal Crude to Chemicals (TC2C<sup>TM</sup>) and Catalytic Crude to Chemicals (CC2C<sup>TM</sup>) technologies.<sup>10,11</sup>

One of the main challenges at hand for OTC technologies is catalyst formulation. Typical cracking catalysts contain a number of components: (i) zeolite/s, (ii) clay, and (iii) binder, which are essential constituting parts of the catalyst body.<sup>5,12–14</sup> The matrix is used to improve several features such as activity, density, and attrition resistance.<sup>15</sup> Generally, cracking is initiated on the acid sites of FCC particles, and therefore the acidity of the FCC components influences the overall cracking activity of the catalyst. Hence, zeolites have

<sup>a</sup> KAUST Catalysis Center (KCC), King Abdullah University of Science and Technology, Thuwal 23955-6900, Saudi Arabia. E-mail: [jorge.gascon@kaust.edu.sa](mailto:jorge.gascon@kaust.edu.sa)<sup>b</sup> Department of Physics-Light-Materials (PLUM), Institute Neel, CNRS UPR2940, France<sup>c</sup> Chemicals R&D, Research and Development Center, Saudi Aramco, Thuwal 23955, Saudi Arabia† Electronic supplementary information (ESI) available. See DOI: <https://doi.org/10.1039/d2cy01125e>

been used in FCC catalyst particles since the 1960s due to their suitable acidic properties.<sup>16–18</sup> Although a wide range of zeolites has been investigated, ultra stable faujasite Y (USY) remains the backbone of industrial FCC catalysis. Y zeolites are responsible for maximizing liquefied petroleum gas (LPG), olefins, and gasoline by primary cracking of heavy paraffins through its characteristic 12MR pore system, providing much of the catalytic activity in a conventional catalyst formulation.<sup>5,19–21</sup> The well-known 10MR ZSM-5 zeolite is added to maximize olefins yield. ZSM-5 can reduce hydrogen transfer activity as a result of steric inhibition of the bulkier transition states typical from bimolecular reactions. Consequently, the small pore size of ZSM-5 favors the monomolecular mechanism and leads to higher selectivity to light olefins, more precisely, to propylene.<sup>5,13,22,23</sup>

Together with USY, ZSM-5 is the second most widely used zeolite in catalytic cracking applications.<sup>24</sup> As we reported earlier, crude oil is mostly cracked on the FAU zeolite up to mid-sized hydrocarbons. Cracked products from the FAU zeolite are the primary reactants for the shape-selective ZSM-5, where the narrow pores of MFI enhance cracking to lower olefins. Our results demonstrate that maintaining a good balance between main base cracking FAU and lower olefins boosts the ZSM-5 additive. Considering conversion, olefins yields, and coke formation, 1:1 wt% of FAU:ZSM-5 ratios seem to be the most suitable combination.<sup>25</sup>

A very important issue for OTC technologies is the development and formulation of catalysts able to handle crude oil at industrial scale. This involves continuous cyclic operation between reaction and regeneration for several hours at high temperatures (500–800 °C) in the presence of steam; where the catalyst particles may be subjected to structural change and irreversible deactivation through processes such as hydrothermal dealumination.<sup>26</sup> An additional concern is the presence of impurities, *i.e.*, nickel, vanadium, nitrogen and sulfur in the crude oil, which lead to catalyst poisoning, thus decreasing catalytic activity and promoting coke formation.<sup>3,27,28</sup> Upon deposition of nickel and vanadium on the catalyst particle, the interaction between the metal and catalyst will lead to a change in the main reaction pathway and enhance dehydrogenation reactions, thus disturbing catalyst selectivity.<sup>29,30</sup> The nature of the zeolites used in the formulation is also expected to play a major role, for instance, ZSM-5 is more tolerant than FAU to metal poisoning by vanadium.<sup>31,32</sup>

A large body of the literature deals with FCC catalyst deactivation. In most of these works, two-step cyclic deactivation (CD)<sup>33,34</sup> and Mitchell impregnation-steam deactivation (MI)<sup>35</sup> are used to mimic the conditions faced by the catalyst during operation. Here, instead of following the classical protocols, in order to get a picture of the actual deactivation rates during the direct cracking of untreated crude oil, we performed long term catalyst reaction-regeneration cycles and studied catalyst evolution under these conditions. In depth characterization of the catalysts at

different stages of their lifetime reveals the main deactivation pathways and mechanism of metal deposition and zeolite dealumination.

## Experimental part

### Materials

Arabian light crude oil (AL) was provided by Saudi Aramco and used in all catalytic experiments without any pre-treatment. The American Petroleum Institute (API) gravity was measured using an Anton Paar DMA 35 instrument following the American Society for Testing and Materials (ASTM) method D7777 (Table 1).

Kaolin was purchased from Sigma-Aldrich. Aluminum chlorohydrate ( $\text{Al}_2(\text{OH})_5\text{Cl}$ ) was purchased from Spectrum. SiC (~800 nm) was supplied by US Research Nanomaterials. The ZSM-5 (MFI) zeolite with  $\text{SiO}_2:\text{Al}_2\text{O}_3$  molar ratios (SAR) of 23 (CBV 2314) and the Y zeolite (FAU) with a SAR of 30 (CBV 720) were purchased from Zeolyst. All zeolites were supplied either in  $\text{H}^+$ - or  $\text{NH}_4^+$  exchanged form.

### Catalyst preparation and shaping

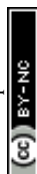
The catalyst formulation (ACM-101) was prepared by admixing clay,  $\text{Al}_2(\text{OH})_5\text{Cl}$  binder precursor (40 wt% in  $\text{H}_2\text{O}$ ), 800 nm SiC, Y and MFI zeolites in deionized water at 20:20:20:20:20 wt% proportion along with 0.1 wt% of phosphorous stabilizer as ammonium phosphate, respectively. Prior to spray drying, the composite slurry was homogenized by ball milling at 350 rpm for 30 min with 2 mm  $\text{ZrO}_2$  grinding media (20 wt% relatives to the total mass of the slurry) as detailed in our previous work.<sup>36,37</sup> Next, the composite slurry was filtered to remove grinding beads and large agglomerates to prevent clogging of the spraying nozzle. The shaping of the catalyst was performed on a laboratory scale spray drying system (Lab-scale Spray Dryer Buchi B-290) applying the following process settings: nozzle diameter ID = 2.0 mm,  $T_{\text{inlet}} = 220$  °C,  $T_{\text{outlet}} = 130$  °C, an airflow of  $35 \text{ m}^3 \text{ h}^{-1}$  and feeding slurry with  $15 \text{ mL min}^{-1}$  rate. The dry product was sieved using calibrated screens with 35  $\mu\text{m}$  and 100  $\mu\text{m}$  apertures to recover a fluidizable fraction composed of spherical particles with diameters lying in the 35–100  $\mu\text{m}$  range. Finally, the catalysts were calcined at 810 °C for 7 h increasing temperature at a  $5$  °C  $\text{min}^{-1}$  rate.

### Characterization methods

**Powder X-ray diffraction.** Powder X-ray diffraction (PXRD) patterns were acquired on a Bruker D8 Advance operated at

**Table 1** Physico-chemical properties of Arabian light crude oil

Density at 15 °C/kg $\text{m}^{-3}$	Gravity/° API	CHN/wt%			ICP-OES/ppm		
		C	H	N	S	Ni	V
846	35.8	79.3	10.7	0.1	17 330	6	14



40 kV and 40 mA an acquisition step size of  $0.1^\circ$  within the  $5\text{--}90^\circ$   $2\theta$  range.

**Nitrogen ( $\text{N}_2$ ) adsorption.** Nitrogen ( $\text{N}_2$ ) adsorption experiments were carried out at 77 K using Micromeritics ASAP 2040 instruments. Before analysis, the composite sample was degassed at  $350^\circ\text{C}$  for 8 h under vacuum conditions. From the obtained isotherms, the specific surface area was calculated using the BET equation ( $S_{\text{BET}}$ ), and the external surface ( $S_{\text{ext}}$ ) and micropore volume ( $V_{\text{micro}}$ ) were calculated by the  $t$ -plot method.

**Temperature-programmed  $\text{NH}_3$  desorption ( $\text{NH}_3$ -TPD).** Temperature-programmed  $\text{NH}_3$  desorption ( $\text{NH}_3$ -TPD) was measured in an AMI-200ip Catalyst Characterization System (Altamira). Approximately 50 mg of the catalyst was first stripped under Ar at  $100^\circ\text{C}$  for 30 min and, then at  $550^\circ\text{C}$  for 90 min to remove volatile components. Then, the sample was saturated with  $\text{NH}_3$  (1.5 vol% in He) at  $120^\circ\text{C}$  for 60 min followed by purging with He flow at  $150^\circ\text{C}$  to remove physisorbed  $\text{NH}_3$ . Finally, the desorption of chemisorbed  $\text{NH}_3$  was monitored by a thermal conductivity detector (TCD) and a MS-detector ( $m/z = 16$  signal attributed to  $\text{NH}_3$ ) applying a ramp from  $150^\circ\text{C}$  to  $650^\circ\text{C}$  at a  $5^\circ\text{C min}^{-1}$  rate. The values for acid site density were calculated by dividing the total acidity by the total BET surface area.

**Pyridine IR (py-IR) measurements.** Transmission FTIR spectroscopy was performed with pyridine being used as a probe molecule in a Nicolet 6700 spectrometer using an MCT/B detector. The sample pellet was prepared using approximately 60 mg of material without any dilution with KBr. After moisture removal under vacuum at  $375^\circ\text{C}$  for 24 h, pyridine vapor was introduced at its vapor pressure under ambient conditions. After saturation, excess pyridine was removed by evacuation at  $150^\circ\text{C}$  for 1 h. Spectra were recorded in the  $1000\text{--}4000\text{ cm}^{-1}$  range at a resolution of  $4\text{ cm}^{-1}$  and co-addition of 64 scans. The amount of Brønsted (BAS) and Lewis (LAS) acid sites were obtained from the bands at  $1545$  and  $1456\text{ cm}^{-1}$  respectively using extinction coefficients of 1.67 and 2.22 (ref. 38) assuming that one molecule of pyridine is adsorbed on one acid site then the following expressions were used to quantify the BAS and the LAS:

$$C_{\text{BAS}} = 1.88 \times \text{IA (B)} \times R^2/W \quad (1)$$

$$C_{\text{LAS}} = 1.42 \times \text{IA (L)} \times R^2/W \quad (2)$$

where IA (B or L) is the integrated absorbance of BAS or LAS band ( $\text{cm}^{-1}$ ),  $R$  is the radius of catalyst disk (cm), and  $W$  is the mass of catalyst (mg).

For thermogravimetric analysis (TGA), the spent catalysts were heated from  $40$  to  $800^\circ\text{C}$ , using a heating ramp of  $10^\circ\text{C min}^{-1}$ , under a nitrogen flow of  $25\text{ mL min}^{-1}$ , to remove all so-called “coke precursors” including minor water adsorption. After half an hour at  $800^\circ\text{C}$  in this inert atmosphere and maintaining the same temperature, the

catalyst was submitted to the airflow of  $25\text{ mL min}^{-1}$ , burning in this way the remaining “hard coke.”

**Temperature programmed oxidation (TPO).** Temperature programmed oxidation (TPO) coke analysis of the spent catalysts was carried out using a TGA/DSC1 STAR-e system apparatus (Mettler Toledo). Prior to TPO experiments, the catalyst was subjected to stripping under  $\text{N}_2$  stream ( $50\text{ mL min}^{-1}$ ) up to the reaction temperature using a heating ramp of  $10^\circ\text{C min}^{-1}$ . After that, the sample was cooled down and stabilized at  $100^\circ\text{C}$ . For the coke combustion step, the temperature was increased up to  $800^\circ\text{C}$  using a heating ramp of  $5^\circ\text{C min}^{-1}$  under an airflow of  $50\text{ mL min}^{-1}$  and kept at  $800^\circ\text{C}$  for 20 minutes so ensure the total coke combustion.

**CHN elemental analyses.** CHN elemental analyses were performed in a Flash 2000 Elemental Analyser CHNS/O by ThermoFisher, using *ca.* 4 mg of sample per analysis and acetanilide as calibrating compound.

**Inductively Coupled Plasma-Optical Emission Spectrometry.** Inductively Coupled Plasma-Optical Emission Spectrometry (ICP-OES) was performed using a 5100 ICP-OES instrument (Agilent) under Ar atmosphere and provided with a SPS 4 Autosampler (Agilent). This technique was used for both natural clays and AL analysis. Digestion was done at  $240^\circ\text{C}$  and 35 bar using UltraWAVE apparatus (Milestone) using an acid mixture of hydrochloric (HCl), nitric ( $\text{HNO}_3$ ), and hydrofluoric acid (HF) mixed at a 6:2:1 volume ratio for clay samples. In the case of AL, solely  $\text{HNO}_3$  was used. Before digestion of the samples, a vessel cleaning step was performed using only nitric acid. A new calibration curve (four plots) was built for each set, and all samples were duplicated except the buffer sample. Moreover, laboratory reagent blank (LRB), laboratory fortified blank (LFB), quality control sample (QCS), and continuing calibration verification (CCV) samples were recorded to validate the results as recommended in several standards methods.<sup>39,40</sup>

**Solid-state Nuclear Magnetic Resonance.** Solid-state Nuclear Magnetic Resonance (ssNMR) experiments were performed on a 14.1 T Bruker Advance III spectrometer, operating at a  $^1\text{Al}$  Larmor frequencies of  $156.37\text{ MHz}$ . The spectra were acquired using a  $3.2\text{ mm}$  probe with  $170\text{ kHz}$   $\pi/2$  pulse and a recovery delay of 0.3 s. The spectra were accumulated from 4096 scans. Typically, the sample was spun using dry nitrogen at a magic angle spinning (MAS) rate of  $20\text{ kHz}$ . The ratio between tetra-, penta- and octahedral Al species was approximately estimated by integration of the spectra as per the corresponding regions, *i.e.*,  $80\text{--}40$ ,  $40\text{--}20$ ,  $20\text{--}0\text{ ppm}$  for  $\text{Al}^{\text{IV}}$ ,  $\text{Al}^{\text{V}}$  and  $\text{Al}^{\text{VI}}$ , respectively.

**Scanning electron microscopy.** Scanning electron microscopy (SEM) was performed using a Field Emission Scanning Electron Microscope (FESEM) from Zeiss Ultra+ (Zeiss, Germany) equipped with an Energy-Dispersive Spectrometers, (EDS – Bruker, France). EDS spectra were obtained on a silicon drift detector Bruker 4010 (SDD). SEM images, EDS spectra and map are obtained at  $20\text{ kV}$  and at  $8\text{ mm}$  working distance. The Electron Probe Microanalyzer for



wavelength-dispersive spectrometry (WDS) is a JEOL 8800 system equipped with 5 spectrometers each carrying two analyser crystals and equipped with gas detectors (P10 or Xe). Analysis were done at 20 kV for Ni (LiFH), V (PETJ or LiFH), Si (PETH) and Al (TAP). Particle surface morphology observations were carried out on an FEI TENE0 VS microscope operated at 2 kV acceleration voltage and at 5 mm working distance using secondary electron scattering mode.

### Steaming and metal deposition

Prior to metals deposition, the calcined catalysts (thereafter referred as ACM-101-C800) were treated under hydrothermal conditions with approx. 90% of steam at 810 °C for 5 h and the resulted catalyst further denoted as ACM-101-S800.

The reaction/regeneration cycles were performed in a multi-zone fluidized bed reactor (MZFBFR).<sup>9</sup> Two batches of 12 and 18 g of hydrothermally treated ACM-101 catalyst were continuously fluidized in the reactor vessel. The reaction was conducted for 4 h at 570 °C in the reaction zone, while the regeneration operated isothermally at 800 °C with a continuous airflow for 4 h. The used Arabian Light contains mainly Ni and V and was fed at rate of 30 mL h<sup>-1</sup>. The reaction/regeneration cycles were performed at different crude oil to catalyst ratios (CTO) to achieve the desired metal contents.

### Catalytic tests

**Catalytic cracking tests.** The catalytic cracking of AL over the formulated catalysts was conducted in a multi-zone fluidized bed reactor, heated by a tubular oven. An AL/water emulsion was feed by using two different Gilson HPLC 307 Pumps and mixing inside an ultrasonic bath at 40 °C. Gas carrier flow (N<sub>2</sub>/He) was controlled by mass flow controllers (Bronkhorst). Reaction products were passed through a system of three condensers in series maintained at room temperature, where the liquid fraction was collected for further analysis. The amount of catalyst tested in the cracking reaction at 570 °C was fixed to achieve comparable catalyst-to-oil ratios (CTO).

Gaseous products were analyzed online by gas chromatography conducted on a Trace 1310 gas chromatograph (Thermo Scientific) with a MolSieve analytical column and thermal conductivity detector for the analysis of He (internal standard) and H<sub>2</sub>, and an Alumina Plot column and FID for the separation analysis of methane and C<sub>2</sub>–C<sub>5</sub> hydrocarbons. The boiling point distribution curves of AL and the liquid products were carried out on a high-temperature Simulated Distillation Analyzer (HT-SIMDIS), connected with liquid nitrogen as described in ASTM D7169.<sup>41</sup> While that, the quantitative analysis of their light distillate fractions (C<sub>5</sub>–C<sub>9</sub>) was implemented on Detailed Hydrocarbon Analyzer-Front End (DHA-FE) by ASTM D7900.<sup>42</sup> Meanwhile, it was used to make corrections to the distillation curve up to 150 °C. Both analyzers were performed on an

Agilent 7890A (Agilent Technologies, USA), equipped with an FID detector, helium as carrier gas, and PTV injector. Calibration standards, reference samples, quality control checks, and nonpolar columns were provided by AC, The Netherlands. All calculations are described in the ESI.†

## Results and discussion

### Catalyst bulk characterization

ACM-101 catalyst formulation, prepared by spray-drying, contains 20 wt% of ZSM-5/23, 20 wt% of FAU/30, 20 wt% of kaolin clay, 20 wt% of aluminum chlorhydrate (as a binder precursor) and 20 wt% of nanometer-sized (~800 nm) silicon carbide. All shaping parameters and preparation steps related to this composite system can be found in our previous works.<sup>9,36,37</sup> The fresh ACM-101 catalyst was subjected to several stages of treatment, starting with calcination at 810 °C for 7 h, followed by hydrothermal treatment with approx. 90% of steam at 810 °C for 5 h, simulating the harshest conditions that can be found during regeneration.<sup>43,44</sup> Metal deposition on the catalysts was implemented through multiple reaction/regeneration cycles with Arabian light crude oil using a multi-zone fluidized bed reactor (MZFBFR).<sup>9</sup> The amount of metals and sulfur deposited on the catalysts after different reaction cycles (ACM-101-M200 representing 0.45 kg of AL over 18 g of catalyst and ACM-101-M400, obtained after feeding 1 kg of AL over 12 g of catalyst) can be found in Table 2.

To elucidate the effect of calcination, steaming and metal deposition on crystallinity and the potential amorphization of the zeolitic components of the catalyst, PXRD analyses were performed on the fresh, calcined, steamed and metal deposited samples (Table 3, Fig. S2†). The PXRD analysis of all catalysts (Fig. S2†) reveals the characteristic diffraction lines attributed to ZSM-5/23 and FAU/30, even for samples exposed to hydrothermal treatment and multiple reaction/regeneration cycles. According to the analyses of peak broadening (based on FWHM values), gradual degradation of both zeolite components occurs as response to the treatment conditions. It is worth noting that the degradation degree of FAU and MFI zeolites fluctuates almost at the same level and becomes greater as the composite undergoes calcination, steaming, and as the accumulation of nickel, vanadium and sulfur advances (Table 3).

The diffraction peak broadening, observable in both zeolite components, indicates the progressive migration of AlO<sub>4</sub> on tetrahedral sites out of the structure to extraframework positions.<sup>45,46</sup> A highly informative tool that allows a comparative evaluation of dealumination degree of

**Table 2** ICP analysis of the formulated catalysts after multiple reaction/regeneration cycles

Catalyst	V (ppm)	Ni (ppm)	S (ppm)	Crude oil/catalyst
ACM-101-M200	232	78	250	25
ACM-101-M400	406	157	430	83





**Table 3** Crystallographic data and results of PXRD analyses for the ACM-101 after different treatment conditions and metal deposition steps

Formulated catalyst	FWHM/ $^{\circ} 2\theta^a$		Unit cell size (UCS)			$x^{Al}/-$		Dealumination $^c$ /%	
	FAU	MFI	FAU		MFI	FAU	MFI	FAU	MFI
			$a/\text{\AA}$	$V/\text{\AA}^3$	$V/\text{\AA}^3$				
ACM-101-C800	0.161	0.168	24.309(5)	14 365(5)	5404(3)	0.040	0.048	20	23
ACM-101-S800	0.166	0.180	24.300(6)	14 349(6)	5399(3)	0.036	0.045	28	27
ACM-101-M200	0.188	0.193	24.287(5)	14 327(5)	5395(2)	0.030	0.042	39	32
ACM-101-M400	0.197	0.205	24.285(4)	14 322(4)	5374(3)	0.029	0.029	42	54

<sup>a</sup> FWHM based on the most intense peak: for FAU – [111] reflection at  $6.29^{\circ} 2\theta$ , for MFI – [101] reflection at  $8.04^{\circ} 2\theta$ . <sup>b</sup> Aluminum content ( $x_{Al}$  molar fraction) in the framework based on the calculation involved unit cell size parameters and  $\text{NH}_3$ -TPD data for pristine zeolite taken as acidity reference (see ESI†). <sup>c</sup> Compared to aluminum fraction in pristine zeolite calcined at  $550^{\circ}\text{C}$  for 5 h ( $1^{\circ}\text{C min}^{-1}$ ).

the zeolite is the unit cell size, whose changes can be followed by PXRD after every treatment stage. Since the Al–O bond is longer ( $\sim 1.74 \text{ \AA}$ ) than Si–O ( $\sim 1.63 \text{ \AA}$ ), as the aluminum sites migrate out from the framework positions weakening framework population of the acid sites, the unit cell size (UCS) decreases. The UCS descriptor for FAU serves the unit cell constant –  $a$  – because of the cubic settings of the framework whereas the UCS for MFI is expressed by unit cell volume (due to orthorhombic settings).<sup>47</sup> Thus, it can be observed from Table 3 that both FAU and MFI UCS decrease gradually after calcination and steaming, suggesting a progressive depletion of framework aluminum under these conditions. Indeed, evaluating aluminum mole fraction ( $x_{Al}$ ) content using UCS data for both zeolites evidences a gradual migration of aluminum from tetrahedral sites to extraframework positions, with a diminishing  $x_{Al}$  of 20–23% and 28–27% upon calcination and steaming, respectively. In turn, the different levels of cumulative Ni, V and S poisoning drop down the UCS values of FAU and MFI further indicating irreversible deactivation of the zeolite due to dealumination process.

In a following step, the textural properties of the catalysts were analyzed by  $\text{N}_2$  physisorption and the results were summarized in Table 4. The hydrothermal treatment results in a 22% and 9% decrease in  $S_{\text{BET}}$  and  $V_{\text{total}}$ , respectively, as showed by comparison with the fresh calcined catalyst.

Low metal deposition, *i.e.*, 230 ppm V and 78 ppm Ni on the catalyst particles, preserved the textural properties, where the  $S_{\text{BET}}$  and  $V_{\text{total}}$  were almost unaltered when compared to the steamed catalyst. The ACM-101-M400 catalyst, with the highest level of deposited metals, shows a noticeable decrease in  $S_{\text{BET}}$  (12%) and  $V_{\text{total}}$  (14%) compared with the steamed sample. A loss in mesopore volume is mainly observed in the vanadium contamination region from 200 to 400 ppm. Sharp drop in external surface area can be explained by restructuring of catalyst components during the multiple repeated reaction/regeneration cycles.<sup>27,31,32</sup>

### Catalyst acidity

In good agreement with the literature,<sup>48</sup> hydrothermal treatment and metal contamination involve a noticeable decrease of the overall concentration of acid sites by 38 and 59% with respect to the fresh calcined catalyst, as illustrated after analysis of ammonia TPD (Table 5 and Fig. 1(a and d)).

**Table 4** Textural properties derived from  $\text{N}_2$  adsorption at 77 K of the formulated catalysts

Catalysts	$S_{\text{BET}}$ , $\text{m}^2 \text{ g}^{-1}$	$S_{\text{ext}}$ , $\text{m}^2 \text{ g}^{-1}$	$V_{\text{total}}$ , $\text{cm}^3 \text{ g}^{-1}$	$V_{\text{micro}}$ , $\text{cm}^3 \text{ g}^{-1}$	$V_{\text{meso}}$ , $\text{cm}^3 \text{ g}^{-1}$
ACM-101-C800	228	74	0.16	0.06	0.10
ACM-101-S800	178	62	0.14	0.05	0.10
ACM-101-M200	186	60	0.15	0.05	0.10
ACM-101-M400	157	39	0.12	0.05	0.07



**Table 5** Acidity analysis of formulated catalyst and catalyst components

Samples	T peak <sup>a</sup> /°C	Total acidity <sup>a</sup> /mmol g <sup>-1</sup>	C <sub>BAS</sub> <sup>b</sup> /μmol g <sup>-1</sup>	C <sub>LAS</sub> <sup>b</sup> /μmol g <sup>-1</sup>
ACM-101-C800	210.5	0.118	n.a.	
ACM-101-S800	222.7	0.073		
ACM-101-M400	214.1	0.054		
FAU/30@810	284.0	0.243	86.4	123.5
FAU/30@810 steamed	223.9	0.029	7.2 (×12)	45.4 (×2.7)
ZSM-5/23@810	218.0	0.296	59.2	401.1
ZSM-5/23@810 steamed	216.6	0.088	28.9 (×2)	83.9 (×4.7)
Kaolin@810	219.5	0.013	2.3	14.7
Kaolin@810 steamed	224.0	0.010	n/a	
Al <sub>2</sub> Cl(OH) <sub>5</sub> binder@ 810	221.2	0.097	n/a	

<sup>a</sup> Concentration of acid sites (AS) derived from NH<sub>3</sub>-TPD. <sup>b</sup> Concentration of Brønsted (BAS) and Lewis (LAS) acid sites derived from pyridine IR spectroscopy.

In order to understand how the catalyst changes acidity during the steaming and the potential benefits of catalyst formulation over stability, we submitted pristine ZSM-5/23, FAU/30 and kaolin to steaming conditions similar to those applied to the shaped catalyst. The individual TPD profiles for the six samples are shown in Fig. 1(b), while the quantified amount of acid sites per sample is summarized in Table 5. Kaolin clay has an almost negligible amount of acid sites. The fresh calcined FAU/30 and ZSM-5/23 samples have a total acid site concentration of 0.243 and 0.296 mmol g<sup>-1</sup>, respectively. After hydrothermal steaming at 810 °C, the acidity was drastically decreased to a 12% and 30% of the initial value for FAU/30@810 and ZSM-5/23@810 respectively, according to NH<sub>3</sub> TPD. Pyridine IR analysis further demonstrates that the amount of BAS and LAS decreases considerably (Table 5). In case of ZSM-5/23, BAS concentration decreased by factor of 2 and LAS by ~5, indicating that ZSM-5/23 is more stable.

Some interesting conclusions can be drawn upon comparing ACM-101 and the individual zeolite components: while for the calcined samples total acidity of ACM-101 equals that of its zeolitic components after correcting for the 20% loading of each zeolite (0.118 mmol g<sup>-1</sup> vs. 0.108 mmol g<sup>-1</sup>), steaming seems to have a much bigger effect on the pristine zeolites than on the formulated catalyst (0.073 mmol g<sup>-1</sup> measured on the formulated catalyst vs. 0.023 mmol g<sup>-1</sup> corresponding to the combination of acidities of the two zeolites after steaming). PXRD analysis (Table 6, Fig. S3†) for FAU/30 shows a slight decrease of UCS upon calcination and, more significantly – after steaming. The aluminum molar fraction ( $x_{Al}$ ) drops from 0.050 down to 0.041 and 0.035 upon calcination and steaming, respectively, showing dealumination levels comparable with those found in formulated composites under similar conditions (Table 3). In contrast, MFI (ZSM-5/23) undergoes a significantly larger drop in UCS upon calcination and steaming. As evidenced by aluminum fraction values estimated from UCS data, the dealumination levels of standalone ZSM-5/23 are considerably higher than those observed for MFI integrated into ACM-101 composite (*vide supra*). These results suggest therefore that formulation protects specially the ZSM-5/23

component from drastic dealumination under harsh steaming conditions and that, most likely, a large part of the preserved acidity in the formulated catalysts comes from the ZSM-5 component.

Finally, we analyzed the zeolite samples by <sup>27</sup>Al ssNMR spectroscopy in order to gain a better understanding on zeolite dealumination. Chemical shifts between –20–20 ppm, 20–40 ppm and 40–80 ppm are assigned to octahedral (Al<sup>VI</sup>), penta-coordinated (Al<sup>V</sup>) and tetrahedral aluminum (Al<sup>IV</sup>) coordination environments. The untreated FAU/30 and ZSM-5/23 samples in Fig. 1(e and f) mainly consist tetrahedral aluminum in zeolite framework with the small peak Al<sup>VI</sup> for the former mentioned. Calcination at 810 °C induces the generation of extra framework Al<sup>VI</sup> and Al<sup>V</sup> for ZSM-5/23, whereas formation of Al<sup>V</sup> is not pronounced for FAU/30 and Al<sup>VI</sup> amount is only becoming slightly higher. The hydrothermal treatment at 810 °C results in almost same Al<sup>IV</sup>:Al<sup>V</sup>:Al<sup>VI</sup> ratio between for both zeolites, where the amount of framework Al<sup>IV</sup> is notably decreasing.

Taking into account drastic changes in acidity and structural transformation in zeolites after calcination and hydrothermal treatment, textural properties could undergo significant modification and induce diffusion problems. Based on N<sub>2</sub> physisorption of calcined and steamed FAU/30 summarized in Table 7, the hydrothermal treatment results in 6.3% and 9.5% increase in  $S_{BET}$  and  $V_{total}$ , respectively, regarding the thermally treated catalyst. In case of ZSM-5/23, surface area decreased by 21% and  $V_{total}$  did not change, however a slight rearrangement in micro- and mesopores happened. Amorphous kaolin clay after calcination possesses both low  $S_{BET}$  and  $V_{total}$ .

Altogether, these results demonstrate that dealumination almost exclusively affects acidic properties (the most important for catalysis), while hardly affecting textural and structural properties. On the other hand, for the shaped catalyst, a bigger effect is observed on textural and structural properties while acidity is better preserved. This can be explained by the migration of kaolin towards the zeolite components, resulting in a partial blocking of the pores along with realumination.



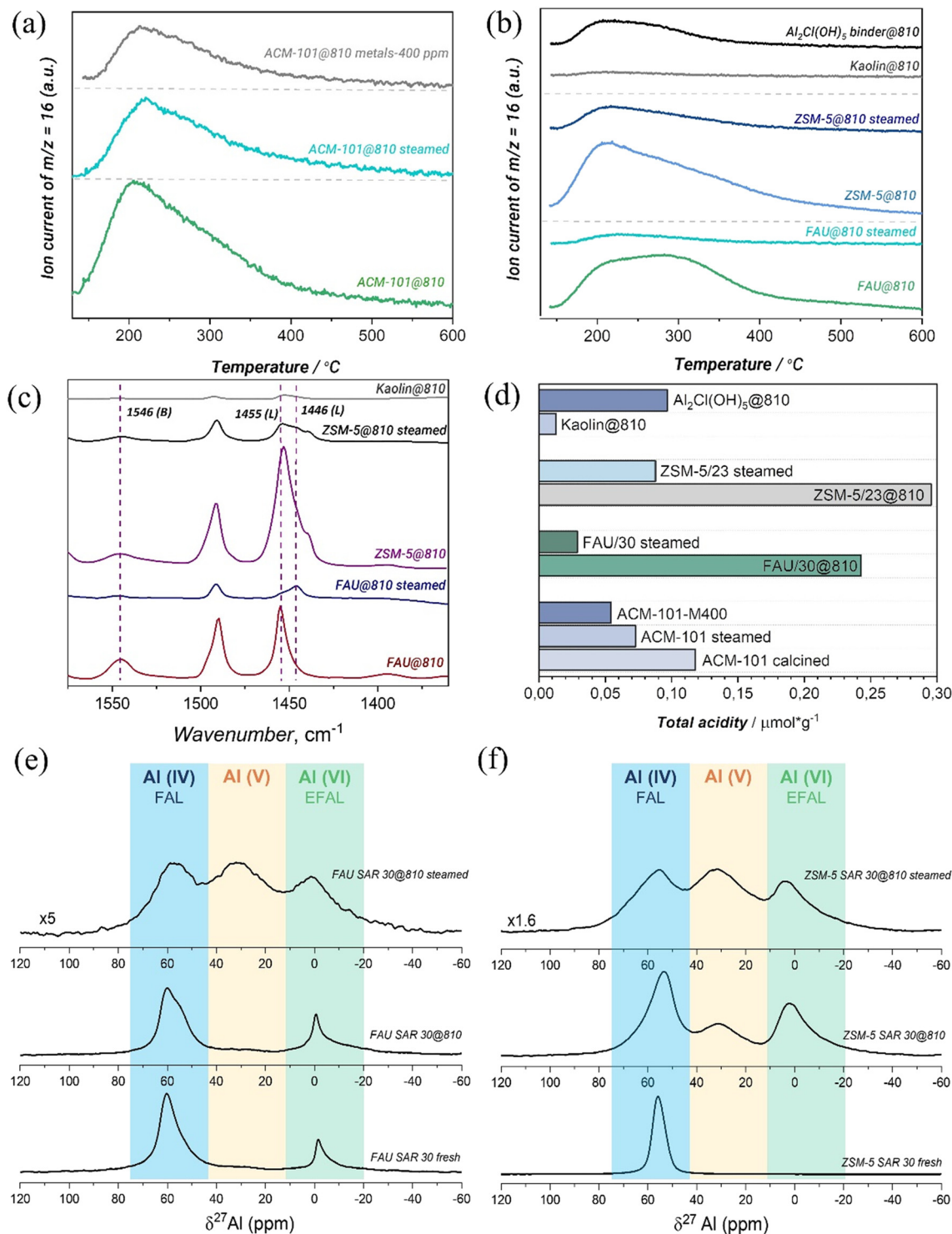


**Fig. 1** NH<sub>3</sub>-TPD profiles of formulated catalyst (a), pristine ZSM-5, FAU zeolites, kaolin and  $Al_2Cl(OH)_5$  binder (b), pyridine IR profiles of formulated catalyst (c) total acidity estimation of formulated catalyst and catalyst components (d), and solid-state NMR spectra of FAU and ZSM-5 zeolites at different stage of treatment (e) and (f) – FAL and EFAL stand for the framework and extraframework aluminum, respectively.

### Particle surface morphology and metal deposition

Topographical characteristics of the ACM-101 catalyst particles at different stages of pretreatment were evaluated using scanning electron microscopy (SEM). As illustrated in

Fig. 2a and b, the calcined (ACM-101-C800) and steamed (ACM-101-S800) features a dense sphere morphology with a surface revealing some roughness due to micron-sized components, predominantly kaolin platelets, sticking out. After fluidization event, that takes place during cracking





**Table 6** Crystallographic data and results of PXRD analyses for FAU and MFI zeolites after different treatment conditions

Components	FWHM/ $^{\circ} 2\theta^a$	Unit cell size (UCS) $^b$	$x_{Al}^{c/-}$	Dealumination $^d/\%$
H-FAU/30 fresh	0.124	24.332(1) Å	0.050	—
FAU/30@810	0.119	24.311(1) Å	0.041	18
FAU/30@810 steamed	0.124	24.297(1) Å	0.035	31
H-ZSM-5/23 fresh	0.147	5425(6) Å <sup>3</sup>	0.062	—
ZSM-5/23@810	0.155	5346(1) Å <sup>3</sup>	0.010	83
ZSM-5/23@810 steamed	0.156	5340(1) Å <sup>3</sup>	0.006	90

<sup>a</sup> FWHM based on the most intense peak: for FAU – [111] reflection at  $6.29^{\circ} 2\theta$ , for MFI – [101]. <sup>b</sup> Unit cell size (UCS) merit for FAU component is  $a$ -unit cell constant (Å), for MFI – unit cell volume (Å<sup>3</sup>). <sup>c</sup> Aluminum content (molar fraction) in the framework based on the calculation involved unit cell size parameters and NH<sub>3</sub>-TPD data for pristine zeolite taken as acidity reference (see ESI†). <sup>d</sup> Compared to aluminum fraction in pristine zeolite calcined at 550 °C for 5 h (1 °C min<sup>-1</sup>).

**Table 7** Textural properties of samples obtained from N<sub>2</sub> uptake measurements at 77 K

Samples	$S_{BET}$ (m <sup>2</sup> g <sup>-1</sup> )	$S_{ext}$ (m <sup>2</sup> g <sup>-1</sup> )	$V_{total}$ (cm <sup>3</sup> g <sup>-1</sup> )	$V_{micro}$ (cm <sup>3</sup> g <sup>-1</sup> )	$V_{meso}$ (cm <sup>3</sup> g <sup>-1</sup> )
FAU/30@810	667	250	0.42	0.17	0.25
FAU/30@810 steamed	709	256	0.46	0.18	0.28
ZSM-5/23@810	422	121	0.24	0.12	0.12
ZSM-5/23@810 steamed	335	143	0.24	0.08	0.16
Kaolin@810	21	21	0.05	—	0.05

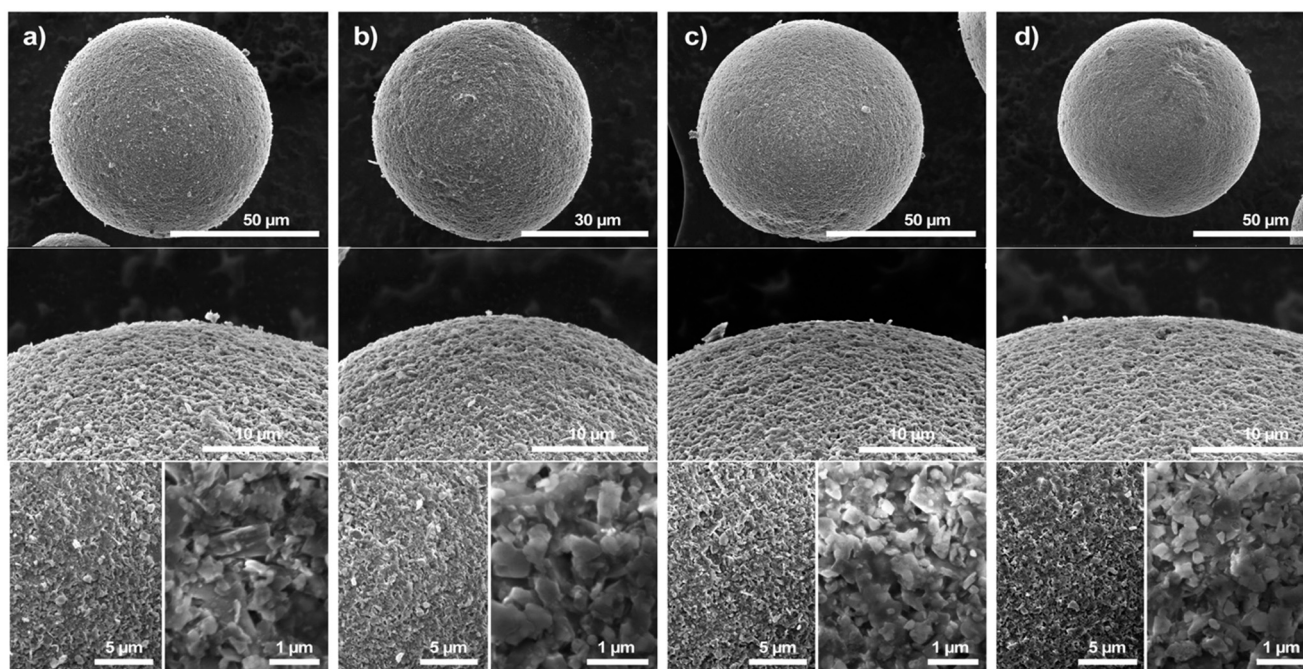


**Fig. 2** SEM surface morphology evaluation of catalyst particles at different stages of pretreatment and accumulated metal content: (a) ACM-101-C800, (b) ACM-101-S800, (c) ACM-101-M200 and (d) ACM-101-M400. The set of images showing different magnification of every catalyst type should be read from the top to the bottom.

process, the catalyst surface becomes smoother as a result of attrition between composite particles (Fig. 2c and d). Particularly, the kaolin platelets, which initially were stuck out of the surface, are rubbed off leading to a sleek surface.

Along with the attrition event, an accumulation of metal contaminants (Ni, V, Fe, etc.) occurs on the catalyst's body during the fluidized bed catalytic cracking process and

evolves gradually over time. Since the content of metal pollutants depend on the duration of a catalytic run, two representative examples, ACM-101-M200 and ACM-101-M400, were examined to unveil any morphological transformation caused by cumulative deposition of poisoning contaminants. As shown in Fig. 2c and d, the catalyst body preserves its pristine shape regardless of the level of metal content. The





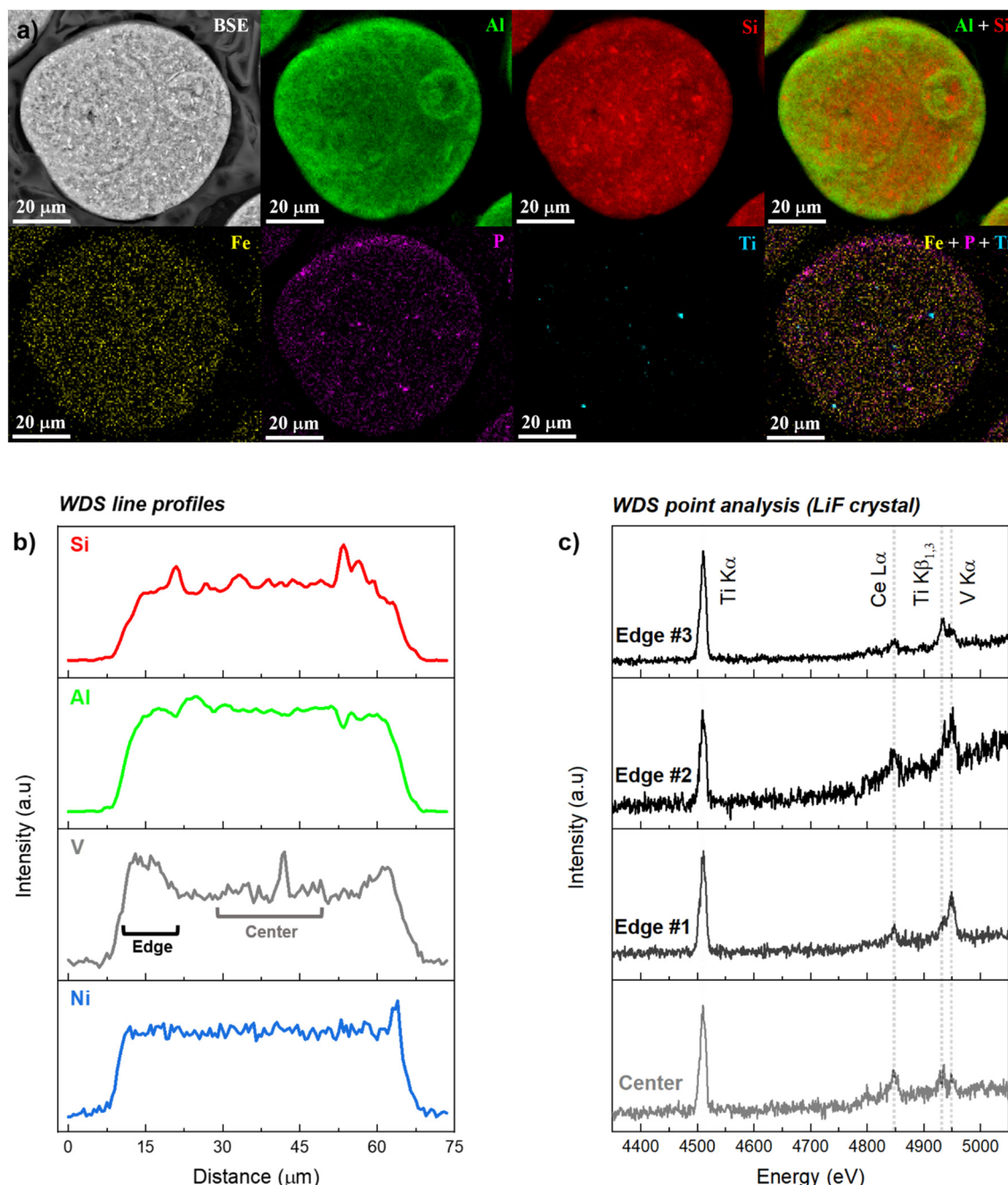


**Fig. 3** a) Backscattered electron image and X-ray maps for the ACM-101-M400 catalyst computed from SEM-EDS data, b) one dimensional analysis of the variation of X-ray intensities from K $\alpha$  fluorescence lines of Si, Al, V, and Ni elements across the particle diameter, c) X-ray fluorescence spectra acquired with a LiF crystal analyzer at the center and at three edges location of a catalyst grain.

absence of nodes or lumps, typically associated with a localized agglomeration of metal oxides on the surface of the catalyst particle, indicates a homogeneous distribution of the poisons over the catalyst body.

Next, we focus on the spent catalyst that contains the largest metal content (ACM-101-M400) to evaluate the distribution of various chemical elements. SEM-EDS data were acquired on a particle cross-section embedded in a conductive resin. Elemental maps were computed from the integration of the K or L fluorescence lines of the most

concentrated elements (Si/Al/Fe/P/Ti). Those chemical maps are displayed on Fig. 3a together with the original micrograph acquired with a back-scattered electron detection. The first observation is related to the morphology of the particle which highlights that the main body corresponds to a fusion of three spherical particles embedded in each other. This suggests that the smallest drops of suspension sprayed by the nozzle are dried before leaving the spraying area, so there is a chance that a subsequent drop of liquid may spread over the surface of



these dried particles, increasing the overall particle size. Interestingly, the drying process resulted also in some segregation of the formulation components. While the distribution of silicon atoms is rather homogenous through the solid at the micrometric scale, the concentration of aluminum atoms is markedly higher at the periphery of the spherical particles (Fig. 3a). Kaolinite from different geological origins have usually variable chemical compositions.<sup>49</sup> Elements, such as Fe, Ti, Mn, Mg and Cr, and impurity phases, such as anatase and mica are often present in natural kaolinites, as the one in use in our current formulation. Predictably, micrometric particles of titanium oxide and iron atoms are found distributed across the particle cross-section as revealed by the titanium and iron maps, respectively. Since iron is well known to substitute aluminum atoms in the crystal structure of kaolinite, the latter can be considered a useful staining marker.<sup>50</sup> This feature would imply that the previous segregation of the aluminum content in the outer layer is most likely due to the alumina binder. Finally, the phosphorous stabilizer added initially in the catalyst formulation is found throughout, although some concentrated spots are noted.

As for metal deposition originating from the crude oil, the low concentration of vanadium and nickel atoms in the spent catalyst (*i.e.* 400 ppm for V and 150 ppm for Ni) prevented any attempts of finding their location by SEM-EDS. To increase our chance of carrying this study, we selected the electron probe microanalysis (EPMA) which rely instead on a wavelength dispersive spectrometer (WDS). This experimental setup has noticeably two advantages over SEM-EDS:<sup>51</sup> i) the energy resolution is largely improved (V-K $\alpha$ :  $\Delta E = 14$  eV with LiF crystal *vs.*  $\Delta E = 150$ –300 eV) and enable for the present study the separation of Ti-K $\beta_{1,3}$  (4966 eV) and V-K $\alpha$  (4953 eV), the enhanced signal to background ratio is favorable to the detection of metal trace amounts (at best down to tenths of ppm). However, these advantages are offset by the long acquisition times that effectively limit – given the low metal concentration – the data acquisition to six-line profiles on different catalyst grains (Fig. S5†). Typical set of line profiles computed from K $\alpha$  line intensities for Si/Al/V/Ni are displayed on Fig. 3b. The silicon and aluminum line profiles are shown to visualize the limits of the catalyst grain. For vanadium, we can therefore conclude that its concentration is higher in the periphery than in the center. For nickel, the line profile would suggest a constant concentration of metal

across the catalyst grain. However, it is not clear whether the fluorescence counts measured within the grain are due to vanadium or nickel alone. It may be an artifact related to an increase in the continuous background as the beam passes from the resin to the catalyst grain. To narrow down these possibilities, we also performed a WDS point analysis on three different edges and in the center of the catalyst grain (Fig. 3c). Thanks to a well resolved observation of the K $\alpha$  line, the resulting spectra further confirms the stronger presence of vanadium at the periphery with a faint contribution in the center. This is in stark contrast to nickel data, for which the K $\alpha$  fluorescence line was found buried in the background irrespective of the analysis location.

### Catalytic activity *vs.* steaming and metal deposition

To evaluate the effect of metal deposition and steaming on the activity of the formulated catalyst catalysts, a series of AL catalytic cracking tests were performed using a multi-zone fluidized bed reactor.<sup>9</sup> Table 8 and Fig. 4 summarize the most important experimental results.

After calcination, ACM-101 leads to around 38 wt% total gas yield (C<sub>1</sub>–C<sub>4</sub> hydrocarbons) with a light olefins (C<sub>2</sub>–C<sub>4</sub>) fraction of *ca.* 27 wt%. Steaming of the catalyst and metal deposition lead to a slight (but not dramatic) loss of activity and to very interesting changes in selectivity patterns: steaming results in a slight decrease of the C<sub>2</sub>–C<sub>4</sub> yield, and into a much more pronounced decrease in the formation of paraffins. This can be explained by the low degree of hydrogen-transfer reactions following a bimolecular reaction mechanism, which can be evaluated by the hydrogen transfer coefficient (HTC =  $(nC_4 + iC_4)/C_{4=}$ ), which decreases with zeolite acid site density<sup>52–54</sup> and probably to the better accessibility of the zeolites upon steaming, which decreases space confinement effects and therefore affects cracking activity.<sup>27,31</sup>

The gradual deposition of metals further affects catalytic performance, although very small differences in activity are found, even for catalysts with over 400 ppm of V and 150 ppm of Ni. Remarkably, even in the presence of metals, the olefin/paraffin ratios are higher and lower HTC values are found. Indeed, GC analysis demonstrates that H<sub>2</sub> yield is increased with the concentration of metal deposited on the ACM-101 catalyst. A similar observation was noted elsewhere.<sup>31</sup> This effect can be attributed to an increase in

**Table 8** Catalytic cracking of AL over ACM-101 using a liquid feed flow of 0.1 mL min<sup>−1</sup> of oil: water (50:50, v/v) and an up-flow stream of 100 mL min<sup>−1</sup> N<sub>2</sub>, 570 °C

Catalyst	C <sub>1</sub> –C <sub>4</sub> <sup>a</sup> /wt%	C <sub>2</sub> –C <sub>4</sub> <sup>b</sup> /wt%	C <sub>3</sub> =/C <sub>2</sub> =	C <sub>2</sub> =/C <sub>2</sub>	C <sub>3</sub> =/C <sub>3</sub>	C <sub>4</sub> =/C <sub>4</sub>	O/P <sup>c</sup>	HTC <sup>d</sup>
ACM-101-C800	35.8	25.5	3.1	3.2	4.9	1.6	2.5	0.61
ACM-101-S800	29.9	23.9	5.2	2.8	9.4	3.9	3.9	0.26
ACM-101-M200	26.1	21.2	5.4	2.6	11.4	4.7	4.3	0.21
ACM-101-M400	26.5	21.5	5.5	2.5	10.5	5.0	4.2	0.20

<sup>a</sup> C<sub>1</sub>–C<sub>4</sub>: average total gas yield. <sup>b</sup> C<sub>2</sub>–C<sub>4</sub>: average total gas yield. <sup>c</sup> O/P: olefin to paraffin ratio. <sup>d</sup> HTC: hydrogen transfer coefficient (HTC =  $(nC_4 + iC_4)/C_{4=}$ ).



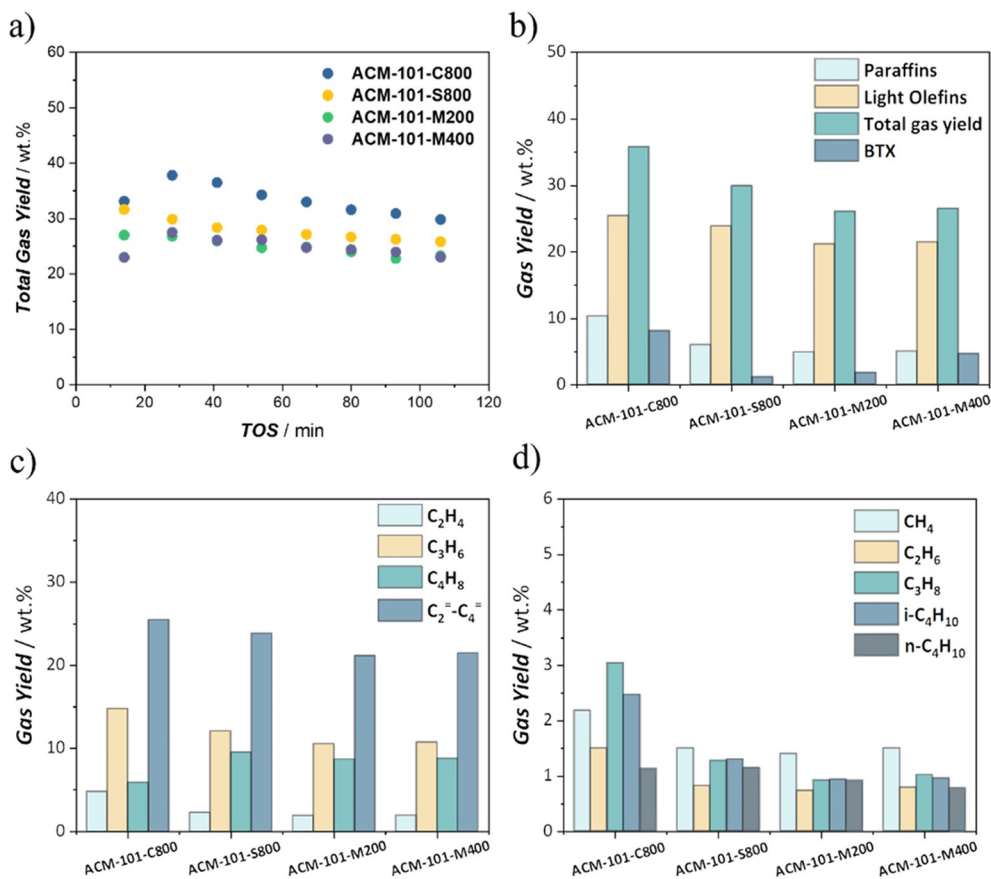


Fig. 4 Catalytic performance of Arabian light over ACM-101 catalysts, stability, and average gas yields of the first hour. (a) Total gas yield; (b) product distribution; (c) olefin distribution and (d) paraffin distribution.

dehydrogenation activity with the deposition of vanadium and nickel.

Distillation curves of AL and liquid fraction after merging with DHA-FE data are displayed in Fig. 5a and the numerical data are summarized in Table S2.† Up to 55% of the liquid product is recovered below 250 °C, which is significantly lower than the original crude oil.

FT-ICR MS analyses showed molecular weight distributions with decreasing average mass/charge ( $m/z$ ) ratios of *ca.* 450, 320, and 325 for the AL crude and the liquid products of ACM-101-S800 and ACM-101-M200, respectively. Consequently, the liquid fraction after catalysis contains a much higher proportion of unsaturated polyaromatic hydrocarbons (carbon # = 20–40, DBE = 10–25) and N and S species than Arabian light (carbon # = 20–40, DBE = 5–12).

The detailed compositions of AL *i.e.*, paraffins, iso-paraffins, naphthenes, and aromatics, before and after catalytic cracking reaction are summarized in Table S3.† *n*-Paraffins are the dominant cracked chemical group among the liquid products. This contributed to the formation of significant amounts of total aromatics (54–41 wt%) and smaller amounts of alkanes, whereas the amount of naphthenes was maintained. As it can be deduced from Fig. 5b, the increased production of BTX with increasing metal concentration relates to the dehydrogenation properties of V and Ni contaminants.<sup>31</sup>

Analysis of the spent catalyst enables us to quantify and identify the nature of the deposited coke and provides information about the deactivation process. Differential thermogravimetry-temperature-programmed oxidation (DTG-TPO) profiles are shown in Fig. 5d, for the spent catalysts after 120 minutes of catalytic cracking of AL at 570 °C. The TPO profiles reveal relatively homogeneous types of coke with a single combustion peak observed in the 400–650 °C temperature range, with maximum combustion rate at *ca.* 530 °C. As reported in the literature, this peak can be related to highly condensed coke.<sup>9,55</sup> Clearly the final amount of coke is related to the acidity of the samples.<sup>56</sup> Furthermore, it is useful to explore the difference between coke precursors, lighter in nature adsorbed and with a higher H content, and hard coke, remnant deposits of highly unsaturated species. Thermogravimetric analysis (TGA) can quantitatively estimate as the hydrocarbon species desorbed in the inert atmosphere during a heating treatment of the spent catalyst in the range of 200–800 °C (coke precursors); and hard coke which removed by combustion at 700–800 °C (Fig. S1†).<sup>57</sup> In FCC-like processes, the presence of both thermal (hard) coke associated with the Conradson carbon residue (CCR) of the feedstock and adsorbed species (coke precursors) is expected.<sup>58</sup> As observed in the figure, while the amount of coke precursors remains fairly constant over the 4 samples,





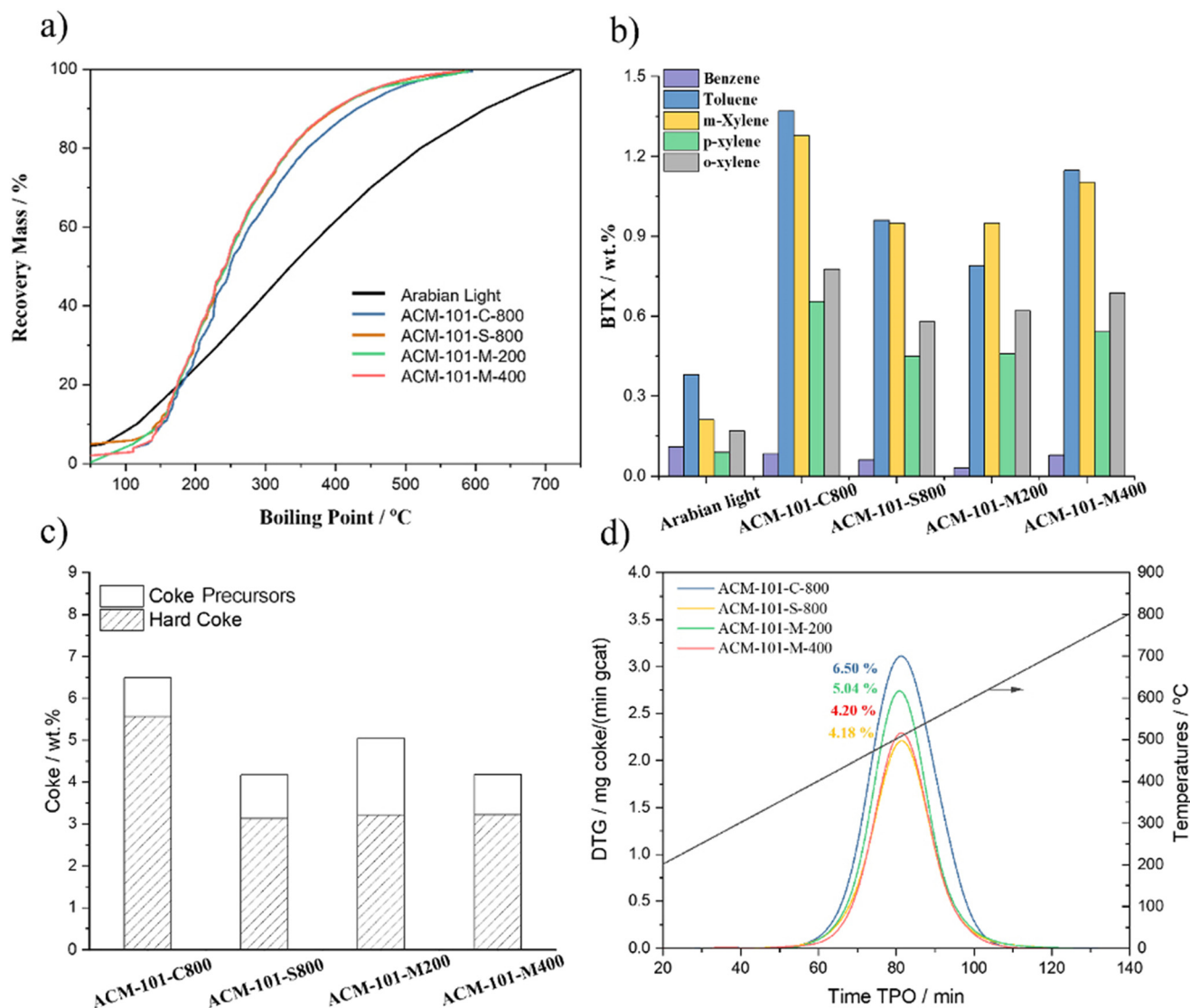


Fig. 5 (a and b) Distillation curves (SIMDIS) (left), and BTXs for liquid fraction collected after catalytic cracking of AL (right). (c and d) Analysis of coke TGA and TPO of spent ACM-101 catalysts.

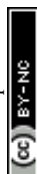
the amount of highly condensed species decreases after steaming of the catalyst, but no further changes are observed upon metal deactivation.

## Conclusion

Catalyst formulation will be key to the industrial deployment of OTC technologies. In this work, we have demonstrated that exposure of zeolite components to conditions similar to those found during catalyst regeneration may lead to an almost complete loss of acidity (and therefore activity). In contrast, catalyst formulation using Al rich matrixes such as kaolin prevents, to a large extent, zeolite dealumination. Interestingly, changes in zeolite acidity during hydrothermal treatment result in enhanced overall selectivity to the main olefins of interest (ethylene and propylene), while the formation of dry gas and saturated gaseous products is decreased. Metal deposition during oil cracking has a similar

effect in terms of selectivity and, in the range studied, does not seem to have a dramatic effect on catalyst activity while slightly improving selectivity thanks to the addition of a dehydrogenation function.

With these results in hand, we estimate that catalyst lifetime in OTC processes should not be different from that found in more classical cracking processes such as FCC: on one hand, the formulated catalysts seem to be able to handle similar metal concentrations in their porosity, on the other hand, neither the presence of sulfur, nor the presence of N containing species seem to pose an issue. In the same line, catalyst regeneration, considering the amount and nature of coke found in the catalysts, is not different from that normally handled in FCC regenerators. Last but not least, if the process of choice involves fluidized bed technologies instead of transport reactors, catalyst attrition should be far less of an issue. Overall, our results further confirm the promise of OTC processes for the efficient production of



olefins and aromatics and may bring the industrialization of such processes one step forward.

## Author contributions

J. G. conceived, designed and supervised the project together with M. A. A., T. S. and A. D. M. A. and A. R. G. performed the catalytic experiments. T. S. and A. D. were responsible for the synthesis, formulation and basic characterization of the catalysts. S. C. and J. R. M. performed the ssNMR analysis and data interpretation. S. O. C., S. P. and J. L. H. performed the advanced catalyst characterization. TGA analyses and coke characterization were performed by I. H. and P. C. Analysis of liquid products was performed by A. O. A. I. M. O., W. X., and K. A. participated in the discussion of results and industrial applicability. The manuscript was drafted by M. A. A., T. S. and J. G. with input from all the authors.

## Conflicts of interest

There are no conflicts to declare.

## References

- World Oil Outlook 2040, The Organization of the Petroleum Exporting Countries, 2019.
- Bp Energy Outlook 2022 Edition, <https://www.bp.com/content/dam/bp/business-sites/en/global/corporate/pdfs/energy-economics/energy-outlook/bp-energy-outlook-2022.pdf>.
- M. A. Alabdullah, A. R. Gomez, J. Vittenet, A. Bendjeriou-Sedjerari, W. Xu, I. A. Abba and J. Gascon, A Viewpoint on the Refinery of the Future: Catalyst and Process Challenges, *ACS Catal.*, 2020, **10**(15), 8131–8140.
- G. M. Wells, *Handbook of Petrochemicals and Processes*, Routledge, Taylor and Francis Group, New York, USA, 1st edn, 1998.
- A. Corma, E. Corresa, Y. Mathieu, L. Sauvanaud, S. Al-Bogami, M. S. Al-Ghrami and A. Bourane, Crude Oil to Chemicals: Light Olefins from Crude Oil, *Catal. Sci. Technol.*, 2017, **7**(1), 12–46.
- I. Markit, Crude Oil-to-Chemicals (Cotc) a Look inside Our Technology & Economic Analyses from the 2019–2014 Process and Economics Program (Pep), 2019.
- A. H. Tullo, Why the Future of Oil Is in Chemicals, Not Fuels, *Chem. Eng. News*, 2019, **97**(8), 20.
- E. Kalinenko and S. Chapman, *New Horizons in COTC, and Refinery and Petrochemical*, Petrochemicals, 2020, <https://europetro.com/media/2020/new-horizons-in-cotc-and-refinery-and-petrochemical>.
- M. Alabdullah, A. Rodriguez-Gomez, T. Shoinkhorova, A. Dikhtiarenko, A. D. Chowdhury, I. Hita, S. R. Kulkarni, J. Vittenet, S. M. Sarathy, P. Castaño, A. Bendjeriou-Sedjerari, E. Abou-Hamad, W. Zhang, O. S. Ali, I. Morales-Osorio, W. Xu and J. Gascon, One-Step Conversion of Crude Oil to Light Olefins Using a Multi-Zone Reactor, *Nat. Catal.*, 2021, **4**(3), 233–241.
- Aramco, Saudi Aramco, Cb&I and Chevron Lummus Global Sign Joint Development Agreement to Demonstrate and Commercialize Thermal Crude to Chemicals (Tc2c™) Technology.
- Aramco, Saudi Aramco, Technipfmc and Axens Advance Catalytic Crude to Chemicals Technology.
- E. T. C. Vogt and B. M. Weckhuysen, Fluid Catalytic Cracking: Recent Developments on the Grand Old Lady of Zeolite Catalysis, *Chem. Soc. Rev.*, 2015, **44**(20), 7342–7370.
- E. T. C. Vogt, G. T. Whiting, A. Dutta Chowdhury and B. M. Weckhuysen, in *Advances in Catalysis*, ed. F. C. Jentoft, Academic Press, 2015, vol. 58, pp. 143–314.
- M. E. Z. Velthoen, A. Lucini Paioni, I. E. Teune, M. Baldus and B. M. Weckhuysen, Matrix Effects in a Fluid Catalytic Cracking Catalyst Particle: Influence on Structure, Acidity, and Accessibility, *Chem. – Eur. J.*, 2020, **26**(52), 11995–12009.
- J. Ruiz-Martinez, I. L. C. Buurmans, W. V. Knowles, D. van der Beek, J. A. Bergwerff, E. T. C. Vogt and B. M. Weckhuysen, Microspectroscopic Insight into the Deactivation Process of Individual Cracking Catalyst Particles with Basic Sulfur Components, *Appl. Catal., A*, 2012, **419–420**, 84–94.
- W. Vermeiren and J. P. Gilson, Impact of Zeolites on the Petroleum and Petrochemical Industry, *Top. Catal.*, 2009, **52**(9), 1131–1161.
- A. Corma, Inorganic Solid Acids and Their Use in Acid-Catalyzed Hydrocarbon Reactions, *Chem. Rev.*, 1995, **95**(3), 559–614.
- J. M. Newsam, The Zeolite Cage Structure, *Science*, 1986, **231**(4742), 1093.
- R. Sadeghbeigi, in *Fluid Catalytic Cracking Handbook (Third Edition)*, ed. R. Sadeghbeigi, Butterworth-Heinemann, Oxford, 2012, pp. 87–115.
- Y. Ghrib, N. Frini-Srasra, E. Srasra, J. Martinez-Triguero and A. Corma, Synthesis of CocrySTALLIZED USY/ZSM-5 Zeolites from Kaolin and Its Use as Fluid Catalytic Cracking Catalysts, *Catal. Sci. Technol.*, 2018, **8**(3), 716–725.
- N. Y. Chen, A. Y. Kam, C. R. Kennedy, A. B. Ketkar, D. M. Nace and R. A. Ware, Catalytic Cracking with a Mixture of Faujasite-Type Zeolite and Zeolite Beta, US7751898A, 1988.
- M. Guisnet, L. Costa and F. R. Ribeiro, Prevention of Zeolite Deactivation by Coking, *J. Mol. Catal. A: Chem.*, 2009, **305**(1), 69–83.
- V. Blay, B. Louis, R. Miravalles, T. Yokoi, K. A. Peccatiello, M. Clough and B. Yilmaz, Engineering Zeolites for Catalytic Cracking to Light Olefins, *ACS Catal.*, 2017, **7**(10), 6542–6566.
- J. Knight and R. Mehlberg, Maximize Propylene from Your Fcc Unit, 2011, 90.
- M. Alabdullah, T. Shoinkhorova, A. Rodriguez-Gomez, A. Dikhtiarenko, J. Vittenet, O. S. Ali, I. Morales-Osorio, W. Xu and J. Gascon, Composition-Performance Relationships in Catalysts Formulation for the Direct Conversion of Crude Oil to Chemicals, *ChemCatChem*, 2021, **13**(7), 1806–1813.
- R. Mallada, in *Encyclopedia of Membranes*, ed. E. Drioli and L. Giorno, Springer Berlin Heidelberg, Berlin, Heidelberg, 2015, pp. 1–2.



- 27 I. L. C. Buurmans, J. Ruiz-Martínez, W. V. Knowles, D. van der Beek, J. A. Bergwerff, E. T. C. Vogt and B. M. Weckhuysen, Catalytic Activity in Individual Cracking Catalyst Particles Imaged Throughout Different Life Stages by Selective Staining, *Nat. Chem.*, 2011, **3**(11), 862–867.
- 28 F. Krumeich, J. Ihli, Y. Shu, W.-C. Cheng and J. A. van Bokhoven, Structural Changes in Deactivated Fluid Catalytic Cracking Catalysts Determined by Electron Microscopy, *ACS Catal.*, 2018, **8**(5), 4591–4599.
- 29 U. J. Etim, B. Xu, P. Bai, R. Ullah, F. Subhan and Z. Yan, Role of Nickel on Vanadium Poisoned Fcc Catalyst: A Study of Physiochemical Properties, *J. Energy Chem.*, 2016, **25**(4), 667–676.
- 30 A. W. Chester, Studies on the Metal Poisoning and Metal Resistance of Zeolitic Cracking Catalysts, *Ind. Eng. Chem. Res.*, 1987, **26**(5), 863–869.
- 31 A. A. Gusev, A. C. Psarras, K. S. Triantafyllidis, A. A. Lappas, P. A. Diddams and I. A. Vasalos, Zsm-5 Additive Deactivation with Nickel and Vanadium Metals in the Fluid Catalytic Cracking (Fcc) Process, *Ind. Eng. Chem. Res.*, 2020, **59**(6), 2631–2641.
- 32 T. F. Degnan, G. K. Chitnis and P. H. Schipper, History of Zsm-5 Fluid Catalytic Cracking Additive Development at Mobil, *Microporous Mesoporous Mater.*, 2000, **35–36**, 245–252.
- 33 M. Bendiksen, E. Tangstad and T. Myrstad, A Comparison of Laboratory Deactivation Methods for Fcc Catalysts, *Appl. Catal., A*, 1995, **129**(1), 21–31.
- 34 A. C. Psarras, E. F. Iliopoulou, K. Kostaras, A. A. Lappas and C. Pouwels, Investigation of Advanced Laboratory Deactivation Techniques of Fcc Catalysts Via Ftir Acidity Studies, *Microporous Mesoporous Mater.*, 2009, **120**(1), 141–146.
- 35 B. R. Mitchell, Metal Contamination of Cracking Catalysts. 1. Synthetic Metals Deposition on Fresh Catalysts, *Ind. Eng. Chem. Prod. Res. Dev.*, 1980, **19**(2), 209–213.
- 36 T. Shoinkhorova, A. Dikhtiarenko, A. Ramirez, A. Dutta Chowdhury, M. Caglayan, J. Vittenet, A. Bendjeriou-Sedjerari, O. S. Ali, I. Morales-Osorio, W. Xu and J. Gascon, Shaping of Zsm-5-Based Catalysts Via Spray Drying: Effect on Methanol-to-Olefins Performance, *ACS Appl. Mater. Interfaces*, 2019, **11**(47), 44133–44143.
- 37 J. Gascon, T. Shoinkhorova, A. Dikhtiarenko, M. Alabdullah, A. Rodriguez Gomez, J. Vittenet, I. Morales Osorio, O. Ali and W. Xu, Metal Carbide Based Catalyst and Method of Making, US17630786, 2022.
- 38 C. A. Emeis, Determination of Integrated Molar Extinction Coefficients for Infrared Absorption Bands of Pyridine Adsorbed on Solid Acid Catalysts, *J. Catal.*, 1993, **141**(2), 347–354.
- 39 Sw-846 Test Method 6010d: Inductively Coupled Plasma-Optical Emission Spectrometry (Icp-Oes), 2018.
- 40 Method 200.7: Determination of Metals and Trace Elements in Water and Wastes by Inductively Coupled Plasma-Atomic Emission Spectrometry, Cincinnati, OH, 1994.
- 41 ASTM D7169-20e1, Standard Test Method for Boiling Point Distribution of Samples with Residues Such as Crude Oils and Atmospheric and Vacuum Residues by High Temperature Gas Chromatography, 2020.
- 42 ASTM D7900-18e1, Standard Test Method for Determination of Light Hydrocarbons in Stabilized Crude Oils by Gas Chromatography, 2018.
- 43 Y. Mathieu, A. Corma, M. Echard and M. Bories, Single and Combined Fluidized Catalytic Cracking (Fcc) Catalyst Deactivation by Iron and Calcium Metal–Organic Contaminants, *Appl. Catal., A*, 2014, **469**, 451–465.
- 44 E. Rautiainen, R. Pimenta, M. Ludvig and C. Pouwels, Deactivation of Zsm-5 Additives in Laboratory for Realistic Testing, *Catal. Today*, 2009, **140**(3), 179–186.
- 45 W. Lutz, Zeolite Y: Synthesis, Modification, and Properties—a Case Revisited, *Adv. Mater. Sci. Eng.*, 2014, **2014**, 724248.
- 46 J. Knöll, U. Singh, J. Nicolich, R. Gonzalez, M. Ziebarth, C. Fouget and S. Brandt, Unit Cell Volume as a Measure of Dealumination of Zsm-5 in Fluid Catalytic Cracking Catalyst, *Ind. Eng. Chem. Res.*, 2014, **53**(42), 16270–16274.
- 47 C. J. Gilmore, J. A. Kaduk and H. Schenk, *International Tables for Crystallography, Volume H: Powder Diffraction*, Wiley, 2019, p. 930.
- 48 V. A. Tsiatouras and N. P. Evmiridis, Fcc Catalysts: Cu(II)-Exchanged Usy-Type. Stability, Dealumination, and Acid Sites after Thermal and Hydrothermal Treatment before and after Vanadium Impregnation, *Ind. Eng. Chem. Res.*, 2008, **47**(23), 9288–9296.
- 49 B.-L. Zhu, C.-L. Qi, Y.-H. Zhang, T. Bisson, Z. Xu, Y.-J. Fan and Z.-X. Sun, Synthesis, Characterization and Acid-Base Properties of Kaolinite and Metal (Fe, Mn, Co) Doped Kaolinite, *Appl. Clay Sci.*, 2019, **179**, 105138.
- 50 P. J. Malden and R. E. Meads, Substitution by Iron in Kaolinite, *Nature*, 1967, **215**(5103), 844–846.
- 51 C. Schwandt, Comparison of Sdd/Wds/Micro-Xrf Element Mapping Methods Using a Garnet Schist Example, *Microsc. Microanal.*, 2010, **16**(S2), 914–915.
- 52 A. Akah and M. Al-Ghrami, Maximizing Propylene Production Via Fcc Technology, *Appl. Petrochem. Res.*, 2015, **5**(4), 377–392.
- 53 J. Meusinger and A. Corma, Influence of Zeolite Composition and Structure on Hydrogen Transfer Reactions from Hydrocarbons and from Hydrogen, *J. Catal.*, 1996, **159**(2), 353–360.
- 54 A. Platon and W. J. Thomson, Low-Temperature Test Reaction for Hydride Transfer on Solid Acid Catalysts, *Catal. Lett.*, 2005, **101**(1), 15–20.
- 55 Á. Ibarra, A. Veloso, J. Bilbao, J. M. Arandes and P. Castaño, Dual Coke Deactivation Pathways During the Catalytic Cracking of Raw Bio-Oil and Vacuum Gasoil in Fcc Conditions, *Appl. Catal., B*, 2016, **182**, 336–346.
- 56 M. Guisnet and P. Magnoux, Organic Chemistry of Coke Formation, *Appl. Catal., A*, 2001, **212**(1), 83–96.
- 57 S. Chen and G. Manos, Study of Coke and Coke Precursors During Catalytic Cracking of N-Hexane and 1-Hexene over Ultrastable Y Zeolite, *Catal. Lett.*, 2004, **96**(3), 195–200.
- 58 M. A. den Hollander, M. Makkee and J. A. Moulijn, Coke Formation in Fluid Catalytic Cracking Studied with the Microriser, *Catal. Today*, 1998, **46**(1), 27–35.

